Zhuo Wang
Department of Mechanical Engineering,
Mississippi State University,
Mississippi, MS 39762
e-mail: zw352@msstate.edu

Pengwei Liu
Department of Mechanical Engineering,
Mississippi State University,
Mississippi, MS 39762;
State Key Laboratory of Advanced Design and
Manufacturing for Vehicle Body,
Hunan University,
Changsha 410082, China
e-mail: liupw789k@hnu.edu.cn

Yaohong Xiao
Department of Mechanical Engineering,
Mississippi State University,
Mississippi, MS 39762
e-mail: yx144@msstate.edu

Xiangyang Cui
State Key Laboratory of Advanced Design and
Manufacturing for Vehicle Body,
Hunan University,
Changsha 410082, China
e-mail: cuixy@hnu.edu.cn

Zhen Hu[1]
Department of Industrial and Manufacturing
Systems Engineering,
University of Michigan,
Dearborn, MI 48128
e-mail: zhennhu@umich.edu

Lei Chen[1]
Department of Mechanical Engineering,
Mississippi State University,
Mississippi, MS 39762;
Department of Mechanical Engineering,
University of Michigan,
Dearborn, MI 48128
e-mail: chen@me.msstate.edu

A Data-Driven Approach for Process Optimization of Metallic Additive Manufacturing Under Uncertainty

The presence of various uncertainty sources in metal-based additive manufacturing (AM) process prevents producing AM products with consistently high quality. Using electron beam melting (EBM) of Ti-6Al-4V as an example, this paper presents a data-driven framework for process parameters optimization using physics-informed computer simulation models. The goal is to identify a robust manufacturing condition that allows us to constantly obtain equiaxed materials microstructures under uncertainty. To overcome the computational challenge in the robust design optimization under uncertainty, a two-level data-driven surrogate model is constructed based on the simulation data of a validated high-fidelity multiphysics AM simulation model. The robust design result, indicating a combination of low preheating temperature, low beam power, and intermediate scanning speed, was acquired enabling the repetitive production of equiaxed structure products as demonstrated by physics-based simulations. Global sensitivity analysis at the optimal design point indicates that among the studied six noise factors, specific heat capacity and grain growth activation energy have the largest impact on the microstructure variation. Through this exemplar process optimization, the current study also demonstrates the promising potential of the presented approach in facilitating other complicate AM process optimizations, such as robust designs in terms of porosity control or direct mechanical property control.
[DOI: 10.1115/1.4043798]

Keywords: additive manufacturing, uncertainty, data-driven, robust design

1 Introduction

Additive manufacturing (AM), which creates 3D components layer-by-layer based on the computer-aided design model, offers a great potential for fabricating component with complex geometry in a cost- and time-saving manner [1–4]. One of the major hurdles for the wide application of AM techniques is the variation in the quality of the manufactured parts [5]. That is, various uncertainty sources exist in the AM process and cause variability in the product quality through uncertainty propagation and aggregation, thus hindering the repetitive manufacturing of products with consistent quality. For example, it has been pointed out that the quality and properties of deposits can vary greatly even when all producers used the same materials, processing parameters, and, in some cases, even the same type of AM machine [6].

Uncertainty quantification (UQ) can help resolve the above issue by constructing product variation as functions of the contributing factors and then making effective uncertainty management (UM). One common strategy is to adjust control factors to dampen the variation caused by noise factors, i.e., type I robust design [7] as illustrated in step 3 in Fig. 1. In the case of the AM process, control factors mainly refer to these AM operating settings, such as preheating temperature, electron beam (EB) power, and scanning velocity. Operators can purposely manipulate them, namely, the process optimization, to minimize variability in product quality caused by random noise factors (uncertainty sources), just like finding out $x = a$ in the simple case shown in Fig. 1. Of course, the robust design in this research is much more complicated than the illustrative case. The product quality has a nonlinear dependence on multiple control factors and noise factors in the AM process, of which the later includes the fluctuating power absorption and various uncertain materials properties, as detailed in Sec. 3.1.

Model-based uncertainty quantification [8–10] especially provides a cheap yet effective way to achieve quality control, with the development of advanced simulation techniques. Current model-based UQ in the AM process is however still at its early stage. Modeling of the entire AM process is a multilevel problem [11]. The product quality is linked to the operating parameters

[1]Corresponding authors.

Manuscript received December 19, 2018; final manuscript received May 7, 2019; published online June 10, 2019. Assoc. Editor: Qiang Huang.

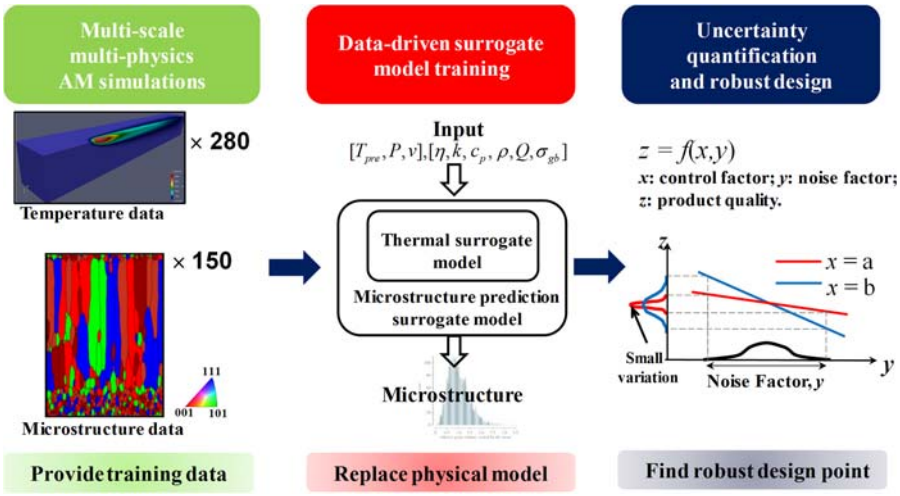

Fig. 1 Workflow of the proposed data-driven approach for uncertainty quantification and management

through multiple connected lower-level models (e.g., powder-bed model and heat source model) and upper-level models (e.g., melt pool model and solidification model). Nonetheless, most of the current UQ analysis are limited to the scope of a single level [6,12–16], especially the variation in the melt pool. Thus, yielding a guideline toward direct quality control by optimizing operating parameters is impossible. For instance, Kamath [12] investigated variability in the melt pool depth associated with uncertain laser parameters. Lopez et al. [13] also studied the geometrical variation of melt pool concerned with uncertain laser and materials properties. A recent study by Haines et al. [14] has revealed the sensitivity of materials microstructure to alloy composition, thus with the focus on grain evolution at the solidification level only. A systematic UQ and UM spanning multilevel of AM process, i.e., correlating process parameters and uncertain sources arising from different level to the final product quality, is still lacking.

The main reason for the absence of a systematic UQ and UM is that few reliable multilevel AM simulation models are currently available to support a model-based multilevel study. Various physical phenomena are involved in the entire AM process, hence greatly inhibiting the development of a high-fidelity AM simulation model. Existing multilevel models [17–20] usually failed to take into account, for example, re-melting phenomenon in a layer-wise building and/or undercooling-controlled grain nucleation. But all of them indeed influence the formation of final grain structure [21–23]. Another reason can be related to the multilevel nature, which indicates a large number of uncertain sources across multiple levels. For a powder-bed AM process, there are dozens of factors that may influence the quality of a final manufactured part [24]. Consequently, extensive simulations at numerous points over a high-dimensional space are required during iterations to find the optimal point. This fact tends to make a multilevel UQ and UM computationally intractable, even with a reliable multilevel simulation model in hand.

In this paper, a data-driven process optimization framework is developed, with application to the uncertainty quantification and management in electron beam melting (EBM) of Ti-6Al-4V. It takes advantage of an advanced multiscale AM simulation model and Kriging surrogate model, allowing effective UQ and UM in a computationally friendly way. Specifically, as shown in Fig. 1, a reasonable number of multiscale multiphysics simulations were first conducted at carefully designed sampling points. This provides training data for training cheap data-driven surrogate models. Through crossvalidation, the surrogate models showed great ability in predicting temperature profile and materials microstructure at a much cheaper computational cost. The surrogate models were then utilized to effortlessly carry out uncertainty quantification and robust design optimization. Based on the UQ analysis, critical factors in affecting the quantity of interest (QoI), here the grain structure described by grain length/width ratio, were successfully identified. Finally, the robust manufacturing condition that makes QoI inert to the variations of noise factors were found, offering manufacturing guidelines to minimize product quality variation.

2 Physical Model

The physical model is based on the combination of our recently developed multiscale multiphysics AM simulation models [25–27]. It spans multilevel by coupling a finite-element (FE)-based heat transfer model for simulating temperature field development and grain growth phase-field model (PFM) for simulating microstructure evolution (more specifically, the prior β-grain structure that largely determines final mechanical properties [28,29] although phase transformation occurs upon cooling below β-transus temperature). In the microstructure simulation, it has accounted for the multiple in-process physical phenomena as mentioned early. Here, we just provide essential aspects of this model, but readers interested in greater detail are referred to Refs. [25–27].

2.1 Finite-Element-Based Heat Transfer Model. During the electron-beam melting process, temperature fields featuring steep thermal gradient are usually formed within and around the moving melt pool, which dictate the final grain structure development. There are mainly two types of thermal models for predicting the temperature field during the AM process, i.e., the analytical model [29–32] (mostly adapted from the early Rosenthal model [33]) and finite-element-based simulation model [27,34,35]. In this multiscale model, a finite-element-based heat transfer model incorporating a moving heat source is utilized to capture the temperature field development during the EBM process. To be specific, the moving heat source, which stems basically from the thermal interaction of the moving electron beam with the deposits, is described by a Gaussian distribution model [20], as follows:

$$Q_e(x,y,z,t) = \eta \cdot P \cdot \frac{4\ln(0.1)}{\pi d^2 z_e} e^{\frac{4\ln(0.1)((x-v\cdot t)^2+y^2)}{d^2}} \left\{ -3\left(\frac{z}{z_e}\right)^2 - 2\left(\frac{z}{z_e}\right) + 1 \right\} \quad (1)$$

where η is the absorptive coefficient of the powder, P is the power of electron beam, d is the electron beam diameter, v is the beam velocity, and z_e is the absolute penetration depth of the electron

beam, calculated by

$$z_e = 2.1 \times 10^{-5} \times \frac{v^2}{\rho} \tag{2}$$

where ρ is the density of the powder materials.

The initial boundary condition is $T = T_{pre}$ applied to the substrate and deposits, where T_{pre} is the preheating temperature. Convective and radiative heat transfers are employed at the surface. Adiabatic conditions are imposed on the sides of the printed part, considering the limited thermal conductivity of loose powders [36,37]. Note that, evaporation is ignored in the current model, as commonly did in AM thermal models [20,34,38]. The above thermal model is realized in ABAQUS with the help of DFLUX user subroutine [39].

Note that, the current thermal model enables us to capture instantaneous temperature field for every microtime step during a layer-by-layer AM process, but fully coupling two models, namely, repeatedly extracting the real-time temperature field and incorporating it into grain growth model, is computationally prohibitive. However, we notice the fact that only the high-temperature field enclosed by the isotherm $T = T_{\beta\text{-}transus}$, here denoted as high-temperature field T_β (x,z) in 2D case, is the useful temperature field for β-grain growth; temperatures below $T_{\beta\text{-}transus}$ are generally believed to have a negligible influence on β grain evolution. As shown in Fig. 2, for most of the time, the aforementioned high-temperature field T_β (x,z) would achieve and remain a relatively steady-state, especially in the bulk section that is exactly of the interest in the current study. By ignoring the short-time unsteady state, the temperature field evolvement is equivalent to a steady temperature field moving along with the electron beam. Also, the steady high-temperature field T_β (x,z) for different layers are assumed to change little under a certain manufacturing condition [40]. As such, once the steady temperature field T_β (x,z) is known, we can easily describe the full temperature field evolvement as T_β $(x\text{-}v\cdot t, z\text{-}n\cdot\Delta h)$ and incorporate it into a grain growth model. In light of this, a thermal surrogate model, which is able to predict the steady temperature field developed under any condition, could be just trained for a fast approximate of the full thermal process. Correspondingly, the FE-based thermal simulation, in this study, is performed mainly to provide training data of stable temperature fields developed under various conditions. To achieve this, simulating a single-layer building is enough and thus adopted in current thermal simulations.

2.2 Thermally Controlled Grain Growth Phase-Field Model. There are various numerical methods existing for the prediction of microstructure during the AM process, including phase-field method [25,41], cellular automaton [42], kinetic Monte Carlo [43], stochastic analysis [34], as well as an analytical microstructural model [44]. Among the simulation models, the phase-field method is especially advantageous in simulating complicated microstructures by avoiding explicitly tracking the evolving interface/boundary [45]. Here, we have greatly elaborated the basic grain growth phase-field model for applicability in simulating grain evolution during the metal-based AM process. For example, the current PFM uses grain boundary energy κ_q that increases with the angle between grain orientation and local thermal gradient ($\kappa_q = \kappa_{q0} \times |\sin\angle(<001>_{axis}, \nabla T)|$), so as to achieve the selective growth of optimally aligned grains essentially due to grains' anisotropy in thermal conductivity, elastic modulus, and surface energy [46]. Also, in order to incorporate the temperature effect on grain boundary mobility, a temperature-dependent grain growth kinetic rate coefficient L_q using a modified Arrhenius type equation is adopted as follows [47,48]

$$L_q(T) = L_0^* \cdot \left(\frac{T}{T_a}\right)^b \cdot \exp\left(-\frac{Q}{R_g T}\right) \tag{3}$$

where T_a is the ambient temperature, R_g is the gas constant of 8.314 J/mol K, L_0^* and b $(-1 < m < 1)$ are the constants, and Q is the activation energy for β-grain growth of Ti-6Al-4V alloy.

Besides the aforementioned selective grain growth and temperature-dependent kinetic rate, various physical phenomena involved in the EBM process are also well incorporated in the phase-field grain growth simulation (see Fig. 2). First, grain growth simulation starts with a pre-existing grain structure serving as the base for building up the layers, which essentially mimics the "starter plate" during Ti-6Al-4V EBM fabrication [49]. The new layers are then periodically added to the substrate, presenting as a layer-by-layer incremental computational domain in the simulation. A physical phenomenon inherent to the layer-by-layer building fashion is the re-melting of previous layers as the electron beam scans the newly deposited powder layer. In the simulation, grain order parameters are intentionally set to 0 as the front edge of the melt pool (i.e., the isotherm line of $T = T_{liquidus}$) is sweeping through and then re-evolve when the trailing edge arrives. Another important phenomenon is the grain nucleation ahead of the solidification front, which is associated with local thermal conditions (i.e., thermal gradient G and solidification rate R). In general, low G/R values at the pool top will result in large constitutional undercoolings that encourage grain nucleation [50,51]. The introduction of new grains would directly interrupt the original epitaxial grain growth and even give rise to equiaxed structures in extreme cases. Regarding its critical role in the microstructure development, a mathematically rigorous treatment of grain nucleation is thus made in this model, as described below.

The total undercooling ΔT consists of the constitutional undercooling ΔT_c, thermal undercooling ΔT_t, generated as the solidification latent heat, and the curvature undercooling ΔT_r. It can be

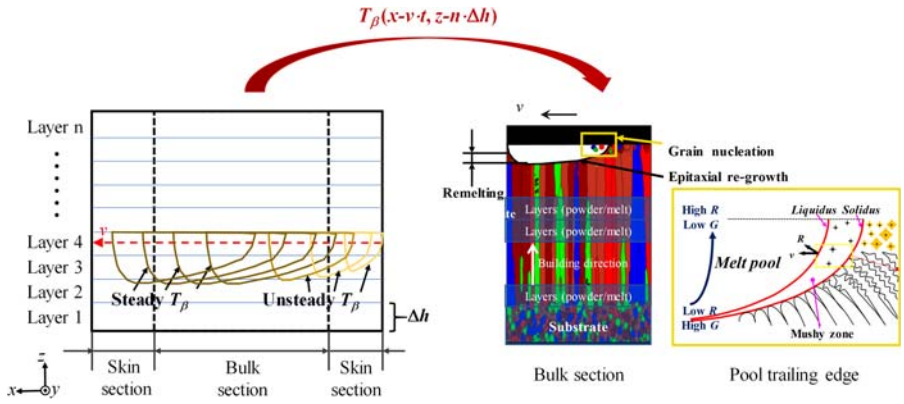

Fig. 2 Schematic illustration of the coupled thermal model and grain growth model

expressed as follows [18]:

$$\Delta T = \Delta T_c + \Delta T_t + \Delta T_r = mC_0(K-1)\left[\frac{I_v(P_c)}{1-(1-k)I_v(P_c)}\right] + \frac{\Delta h_v}{c_p} I_v(P_t) + \frac{2\Gamma}{r} \tag{4}$$

where m represents the liquidus slope, K is the solid/liquid partition coefficient, Δh_v is the fusion enthalpy per unit volume, c_p is the specific heat, and Γ represents the Gibbs–Thomson coefficient. The Ivantsov function $I_v(P) = P\exp(P)E(P)$ and the $E(P) = \int_P^\infty \exp(-t)/t dt$. $P_c = rR/2D$ and $P_t = rR/2h$ are, respectively, the solutal and thermal Peclet numbers, associated with the solute diffusion coefficient in the liquid D, the thermal diffusivity of the melt h, and the dendrite tip radius r, which is a function of a thermal gradient G [19]. Once the local undercooling is calculated with the local thermal condition informed by the as-coupled temperature field, a Gaussian distribution [52] is used to characterize the density of nucleation as a function of undercooling

$$n(\Delta T) = \int_0^{\Delta T} \frac{dn}{d\Delta T'} d\Delta T' = \int_0^{\Delta T} \frac{n_{\max}}{\Delta T_\sigma \sqrt{2\pi}} \exp\left[-\frac{1}{2}\left(\frac{\Delta T' - \Delta T_N}{\Delta T_\sigma}\right)\right] d\Delta T' \tag{5}$$

where ΔT_N and ΔT_σ are the mean undercooling and standard deviation of undercooling, respectively, $n_{\max}$ is the maximum density of nucleation sites. Then, the probability of nucleation at each lattice site can be written as

$$P_v = \delta n_v V_{ea} = \{n[\Delta T(t)] - n[\Delta T(t-\Delta t)]\} dx^3 \tag{6}$$

where $V_{ea} = dx^3$ is the effective volume of each lattice site. A random number r_a within [0, 1] is generated by the computer at lattice sites within the mushy zone in each time step, and a new nucleus is formed at lattice sites where $r_a \le P_v$. In this work, the $n_{\max}$ is 9.0×10^9 m^{-3}, the ΔT_N is 42 K, and the ΔT_σ is 3.0 K for Ti-6Al-4V, through an estimation with author's domain knowledge, followed by trial-and-error calibrations against previous critical G/R line for nucleation happening [23,53,54]. Other parameters used just follow standards in previous work, as listed in Table 1.

The above grain growth model enables us to get grain microstructure and detailed morphology developed under any condition. However, in this research, the grain length/width distribution, i.e., the mean and second moment of grain length/width ratio, is just selected as the microstructure descriptor to facilitate the surrogate model training. Therefore, the grain length/width ratio information would be further extracted as training data after microstructure obtainments. This is expected to correspondingly train a microstructure surrogate model that can quickly predict the grain's length/width ratio distribution and thus the approximate grain structure.

Table 1 Parameters used in the grain growth phase-field model [55–58]

Parameter	Value
Liquidus slope, m (K/wt%)	−0.088
Solid/liquid partition coefficient, K	0.838
Initial alloy concentration, C_0 (/wt%)	10
Enthalpy of fusion, Δh_v (J/mol)	3.71×10^4
Solute diffusion coefficient in the liquid, D (m^2/s)	9.5×10^{-9}
Thermal diffusivity of the melt, h (m^2/s)	6.0×10^{-6}
Gibb–Thomson coefficient, Γ (K m)	1.88×10^{-7}
Liquidus temperature, $T_{liquidus}$ (K)	1928
Solidus temperature, $T_{solidus}$ (K)	1878
β phase transus temperature, $T_{\beta\text{-}transus}$ (K)	1268

Table 2 Variation of different noise factors

Noise factors	Power absorption, η [35,49]	Grain boundary energy, σ_{gb} (J/m^2) [64,65]	Grain growth activation energy, Q (kJ) [66–68]
Lower bound	0.6	0.8	100
Upper bound	0.9	0.9	170

3 Process Parameter Optimization Under Uncertainty

3.1 Uncertainty Sources. Various uncertainty sources or noise factors exist during the metal-based additive manufacturing process. A good example is the fluctuation of power absorption. Power absorption efficiency depends highly on absorbing surface associated with powder packing [59] as well as melt pool dynamics or flow behavior [60,61], both of which however show very random and unstable nature. This fact brings in the power absorption great uncertainty. For example, the energy absorption coefficient assumed in previous researches exhibits large difference, from 0.6 [49] to 0.9 [35], both for the electron beam melting of Ti-6Al-4V using Arcam® S12 machine. Other uncertainty sources include variation of materials properties of powder particles, natural variability in the temperature boundary condition, etc. [62].

In this study, the following uncertainty sources are considered:

- Fluctuation of the power absorption coefficient of powder layers η
- and uncertain materials properties of Ti-6Al-4V powders, including the thermal conductivity k, specific heat capacity c_p, density ρ, grain boundary energy σ_{gb}, and thermal activation energy of grain growth Q.

They all possess great potential for causing great variability in the material's microstructure, through directly affecting grain evolution (i.e., σ_{gb} and Q) or influencing the development of temperature field/melt pool that governs grain evolution. Note that, the manufacturing settings, such as EB power and speed, are usually precisely controlled by advanced control algorithms. Thus, they are considered as controllable parameters with negligible fluctuations in this study. As shown in Table 2, the reasonable variation range of most noise factors are estimated based on different values used in previous researches. It is noted that thermal conductivity, specific heat capacity, and density are temperature-dependent (usually fitted as cubic polynomial relations $a_0 + a_1T + a_2T^2 + a_3T^3$

Table 3 Distribution parameters of the coefficients of the polynomial functions

Noise factors	Thermal conductivity, k (W/m K)		Specific heat capacity, c_p (J/kg K)		Density, ρ (kg/m^3)	
	a_{10}	a_{11}	a_{20}	a_{21}	a_{30}	a_{31}
Mean	4.97	4.95×10^{-3}	531.11	1.19×10^{-1}	4.22×10^3	6.15×10^{-1}
Standard deviation	0.20	0.03×10^{-3}	10	0.24×10^{-2}	40	0.05×10^{-1}

Table 4 Distribution information of some random variables

Noise factors	η	σ_{gb}	Q
Distribution type	Gaussian	Gaussian	Lognormal
Mean	0.75	0.85	130
Standard deviation	0.02	0.01	6

[25,63]), uncertainties of them in this study are thus described by variations in coefficients a_0 and a_1 of the respective polynomial function.

Based on the above observations of the variations of different variables, Gaussian distributions are assumed for the coefficients (i.e., a_0 and a_1) of the polynomial functions of the thermal conductivity, specific heat capacity, and density. The mean values are the maximum likelihood estimates of the coefficients, and the standard deviations are determined by analyzing the confidence intervals of these coefficients using the data provided in Refs. [25,69]. Table 3 gives the distribution parameters of these polynomial function coefficients. Following that, Table 4 presents the assumed distributions of η, σ_{gb}, and Q. The distribution parameters of these three parameters are determined according to the variation intervals presented in Table 2. The distributions of different random variables given in Tables 3 and 4 are used only for illustration purpose since the currently available data are too less to determine an accurate distribution. Note that the focus of this paper is to demonstrate the data-driven framework for robust design optimization of process parameters for given uncertainty sources. The proposed framework is not limited to the assumed distributions. More accurate distributions can be used to model these uncertainty sources when related experimental data are available. Using actual field data to model the random variables instead of assuming certain distributions should be pursued in future work.

Next, we discuss how to perform robust design optimization of the process parameters based on the above information of the uncertainty sources.

3.2 Design Objective. Materials microstructure is the quantity of interest in this study. In general, the equiaxed grain structure exhibits preferable mechanical performance compared to the columnar grain structure. For example, fine equiaxed microstructures can more easily accommodate strain and promote tearing [70]. In contrast, large columnar grain structure usually leads to property anisotropy, premature failure under transverse loading, and shorter fatigue life [2,28]. Thus, the design objective in this study is to find out optimal AM process parameters, which enable us to constantly obtain an equiaxed grain structure under the existence of various uncertainties.

Specifically, grain structure in this research is described using the length/width ratio of grains r, which equals 1 for a perfectly equiaxed grain and takes a much larger value for a columnar grain. The objective of design optimization is thus to move the mean value of r closer to one and minimize the standard deviation of r at the same time. Using this objective function, we then formulate the robust design optimization model as below:

$$\begin{aligned} &\min_{\mathbf{d}} \; w_1(\mu_r(\mathbf{d})-1)^2+(1-w_1)\sigma_r^2(\mathbf{d}) \\ &\text{Subject to} \\ &\mathbf{d}=[T_{pre},\, P,\, v] \\ &\mathbf{d}_L \le \mathbf{d} \le \mathbf{d}_u \end{aligned} \tag{7}$$

where $\mathbf{d}$ is a vector of design variables, $\mathbf{d}_L$ and $\mathbf{d}_u$ are, respectively, the lower and upper bound of the design variables, T_{pre} is the preheating temperature, P is the EB power, v is EB scanning speed, $\mu_r(\mathbf{d})$ and $\sigma_r(\mathbf{d})$ are, respectively, the mean and standard deviation of the length to width ratio, in terms of grains of various materials microstructures developed under the manufacturing condition $\mathbf{d}$, and w_1 is the weight of the mean value in robust design. $w_1=0.5$ in this paper since equal weights are assigned to the mean and standard deviation of r.

For given $\mathbf{d}$, $\mu_r(\mathbf{d})$ and $\sigma_r(\mathbf{d})$ are given by

$$\mu_r(\mathbf{d})=\int_0^\infty r f_{r,\mathbf{d}}(r)dr \tag{8}$$

$$\begin{aligned} \sigma_r^2(\mathbf{d}) &= \int_0^\infty (r-\mu_r(\mathbf{d}))f_{r,\mathbf{d}}(r)dr \\ &= \int_0^\infty r^2 f_{r,\mathbf{d}}(r)dr-\left(\int_0^\infty r f_{r,\mathbf{d}}(r)dr\right)^2 \end{aligned} \tag{9}$$

in which $f_{r,\mathbf{d}}(r)$ is the probability density function (PDF) of r for given $\mathbf{d}$.

Equations (8) and (9) show that our design objective is achieved through controlling both mean and variance of r. With updating $\mathbf{d}$ in Eq. (7), the mean $\mu_r(\mathbf{d})$ is driven to approach 1 indicating the acquirement of equiaxed grain structures, while the standard deviation $\sigma_r(\mathbf{d})$ at the same time is minimized to further ensure uniform grain structure for each product and minimal structure difference among products. As such, the robust design point eventually obtained $\mathbf{d}_{robust}$ would correspond to the optimal manufacturing condition that allows the fabrication of products with consistently equiaxed grain structures.

3.3 Evaluation of the Objective Function. The PDF $f_{r,\mathbf{d}}(r)$ is the unconditional PDF of r by considering various uncertainty sources including not only the uncertainty sources discussed in Sec. 3.1 but also the natural variability of r over a structure for a given realization of the uncertainty sources. Or in other words, r over a structure is a random variable due to the natural variability of microstructure over the structure (see Fig. 7), even if we fix the uncertainty sources at a specific point. $f_{r,\mathbf{d}}(r)$ is unknown to us and needs to be obtained based on the uncertainty propagation of the uncertainty sources. Defining the random variables in the manufacturing process as $\boldsymbol{\theta}=[\eta,\, \sigma_{gb},\, Q,\, a_{10},\, a_{11},\, a_{20},\, a_{21},\, a_{30},\, a_{31}]$, for given $\mathbf{d}$ and $\boldsymbol{\theta}$, we then have

$$f_{r,\mathbf{d}}(r)=\int f_{r,\mathbf{d}}(r|\boldsymbol{\theta})f_{\boldsymbol{\theta}}(\boldsymbol{\theta})d\boldsymbol{\theta} \tag{10}$$

and

$$\mu_r(\boldsymbol{\theta},\,\mathbf{d})=\int_0^\infty r f_{r,\mathbf{d}}(r|\boldsymbol{\theta})dr \tag{11}$$

where $f_{r,\mathbf{d}}(r|\boldsymbol{\theta})$ and $\mu_r(\boldsymbol{\theta},\ \mathbf{d})$ are the conditional PDF and mean of r for given $\boldsymbol{\theta}$ and $f_{\boldsymbol{\theta}}(\boldsymbol{\theta})$ is the joint PDF of $\boldsymbol{\theta}$.

Plugging Eq. (10) into Eq. (8) yields

$$\mu_r(\mathbf{d})=\int_0^\infty r\int f_{r,\mathbf{d}}(r|\boldsymbol{\theta})f_{\boldsymbol{\theta}}(\boldsymbol{\theta})d\boldsymbol{\theta}\,dr=\int\mu_r(\boldsymbol{\theta},\,\mathbf{d})f_{\boldsymbol{\theta}}(\boldsymbol{\theta})d\boldsymbol{\theta} \tag{12}$$

The above equation can be approximated using Monte Carlo simulation (MCS)-based method as

$$\mu_r(\mathbf{d})=\int\int_0^\infty r f_{r|\boldsymbol{\theta},\mathbf{d}}(r)f_{\boldsymbol{\theta}}(\boldsymbol{\theta})dr\,d\boldsymbol{\theta}\approx\frac{1}{n_{MCS}}\sum_{i=1}^{n_{MCS}}\mu_r(\boldsymbol{\theta}^{(i)},\,\mathbf{d}) \tag{13}$$

in which n_{MCS} is the number of MCS samples of $\boldsymbol{\theta}$ and $\boldsymbol{\theta}^{(i)}$ is the ith MCS sample.

Similarly, we have $\sigma_r^2(\mathbf{d})$ as follows

$$\begin{aligned}\sigma_r^2(\mathbf{d}) &= \int\int_0^\infty r^2 f_{r|\boldsymbol{\theta},\mathbf{d}}(r) f_{\boldsymbol{\theta}}(\boldsymbol{\theta}) dr\, \mathbf{d}\boldsymbol{\theta} - \mu_r^2(\mathbf{d}) \\ &= \int\int_0^\infty r^2 f_{r|\boldsymbol{\theta},\mathbf{d}}(r) dr\, f_{\boldsymbol{\theta}}(\boldsymbol{\theta}) \mathbf{d}\boldsymbol{\theta} - \mu_r^2(\mathbf{d}) \\ &= \int m_{r2}(\boldsymbol{\theta}, \mathbf{d}) \mathbf{d}\boldsymbol{\theta} - \mu_r^2(\mathbf{d})\end{aligned} \tag{14}$$

where $m_{r2}(\boldsymbol{\theta}, \mathbf{d}) = \int_0^\infty r^2 f_{r,\mathbf{d}}(r|\boldsymbol{\theta}) dr$ is the second moment of r.

Using the MCS samples of $\boldsymbol{\theta}$, Eq. (14) is approximated as

$$\sigma_r^2(\mathbf{d}) \approx \frac{1}{n_{MCS}} \sum_{i=1}^{n_{MCS}} m_{r2}(\boldsymbol{\theta}^{(i)}, \mathbf{d}) - \left(\frac{1}{n_{MCS}} \sum_{i=1}^{n_{MCS}} \mu_r(\boldsymbol{\theta}^{(i)}, \mathbf{d}) \right)^2 \tag{15}$$

Combining Eqs. (13), (15), and (7), the robust design optimization model can be rewritten as

$$\begin{aligned}\min_{\mathbf{d}}\ & w_1 \left(\frac{1}{n_{MCS}} \sum_{i=1}^{n_{MCS}} \mu_r(\boldsymbol{\theta}^{(i)}, \mathbf{d}) - 1 \right)^2 + (1 - w_1) \\ & \left[\frac{1}{n_{MCS}} \sum_{i=1}^{n_{MCS}} m_{r2}(\boldsymbol{\theta}^{(i)}, \mathbf{d}) - \left(\frac{1}{n_{MCS}} \sum_{i=1}^{n_{MCS}} \mu_r(\boldsymbol{\theta}^{(i)}, \mathbf{d}) \right)^2 \right]\end{aligned} \tag{16}$$

Subject to

$\mathbf{d} = [T_{pre}, P, v]$

$\mathbf{d}_L \le \mathbf{d} \le \mathbf{d}_u$

The above equation indicates that in order to evaluate the objective function, $\mu_r(\boldsymbol{\theta}^{(i)}, \mathbf{d})$ and $m_{r2}(\boldsymbol{\theta}^{(i)}, \mathbf{d})$ need to be evaluated repeatedly with $i = 1, 2, \ldots, n_{MCS}$ for given $\mathbf{d}$. A straightforward way of estimating $\mu_r(\boldsymbol{\theta}^{(i)}, \mathbf{d})$ and $m_{r2}(\boldsymbol{\theta}^{(i)}, \mathbf{d})$ is to perform the multiscale multiphysics AM simulation (as discussed in Sec. 2) by fixing the random variables $\boldsymbol{\theta}$ at $\boldsymbol{\theta}^{(i)}$. In that case, the computationally expensive AM simulations need to be performed n_{MCS} times to get an evaluation of the objective function for a given $\mathbf{d}$. This makes physics-based robust design of process parameters computationally intractable. In this paper, the data-driven surrogate models are employed to overcome the computational challenges in the robust design optimization.

3.4 Data-Driven Surrogate Models. Considering that both the melt pool and microstructure simulation models (see Sec. 2) are computationally expensive, we build two separate surrogate models to substitute the original simulation models based on the simulation data obtained from AM simulations. In this paper, the Kriging surrogate modeling method [71] is employed to build the surrogate models, since Kriging can effectively capture the nonlinearity of the underlying models and can accommodate the noise in the data. For the sake of explanation, we partition the random variables $\boldsymbol{\theta} = [\eta, \sigma_{gb}, Q, a_{10}, a_{11}, a_{20}, a_{21}, a_{30}, a_{31}]$ into two groups, namely $\boldsymbol{\lambda} = [\lambda_1, \lambda_2, \ldots, \lambda_7] = [\eta, a_{10}, a_{11}, a_{20}, a_{21}, a_{30}, a_{31}]$ which are the random variables in the melt pool model and $\boldsymbol{\omega} = [\omega_1, \omega_2] = [\sigma_{gb}, Q]$ which are the random variables in the microstructure model. In what follows, we provide more details of the surrogate modeling of the AM models.

3.4.1 Surrogate Modeling of Steady Temperature Field. For given $\mathbf{d}$ and $\boldsymbol{\lambda}$, the thermal response is a high-dimensional field response. This makes the surrogate modeling of developed steady temperature field challenging. To overcome this challenge, a singular value decomposition (SVD)-based Kriging surrogate modeling method presented in Ref. [5] is adopted in this paper for the thermal surrogate modeling. Figure 3 presents the overall flowchart of the thermal surrogate modeling using the SVD-based Kriging surrogate modeling method.

Define the steady temperature field for given $\mathbf{d}$ and $\boldsymbol{\lambda}$ as $T(\mathbf{d}, \boldsymbol{\lambda}, \mathbf{s})$, where $\mathbf{s} \in \Omega_{xyz}$ stands for all the spatial coordinates of the nodes, we first generate N_t training points for $\mathbf{d}$ and $\boldsymbol{\lambda}$ using Latin Hypercube sampling approach [72] (see Fig. 3). We then perform thermal simulation for each of the training points and obtain the steady temperature field developed under different conditions, $T(\mathbf{d}^{(i)}, \boldsymbol{\lambda}^{(i)}, \mathbf{s})$, $i = 1, 2, \ldots, N_t$. After that, we approximate the original simulation data matrix using SVD as follows [73]:

$$T(\mathbf{d}^{(i)}, \boldsymbol{\lambda}^{(i)}, \mathbf{s}) \approx \sum_{j=1}^{m} \gamma_j(i) \boldsymbol{\eta}_j(\mathbf{s}), \quad \forall i = 1, 2, \ldots, N_t \tag{17}$$

where $\gamma_j(i)$, $i = 1, 2, \ldots, N_t$, $j = 1, 2, \ldots, m$ are the responses in the latent space, m is the number of important features used in SVD, and $\boldsymbol{\eta}_j(\mathbf{s})$, $j = 1, 2, \ldots, m$ are the important features.

Using the training points of $\mathbf{d}$ and $\boldsymbol{\lambda}$ and the corresponding latent space response, we then build surrogate models in the latent space as

$$\gamma_j = \hat{g}_j(\mathbf{d}, \boldsymbol{\lambda}), \quad j = 1, 2, \ldots, m \tag{18}$$

For any new prediction point $\mathbf{d}$ and $\boldsymbol{\lambda}$, we have $\gamma_j(i) \approx \hat{g}_j(\mathbf{d}^{(i)}, \boldsymbol{\lambda}^{(i)})$, and thus the surrogate models are used to predict the steady temperature field response at new prediction point as below

$$\hat{T}(\mathbf{d}, \boldsymbol{\lambda}, \mathbf{s}) \approx \sum_{j=1}^{m} \mu_{\hat{g}_j}(\mathbf{d}, \boldsymbol{\lambda}) \boldsymbol{\eta}_j(\mathbf{s}) \tag{19}$$

where $\mu_{\hat{g}_j}(\mathbf{d}, \boldsymbol{\lambda})$ is the mean prediction of the jth latent space surrogate model and $\hat{T}(\mathbf{d}, \boldsymbol{\lambda}, \mathbf{s})$ is the predicted temperature field response for given $\mathbf{d}$ and $\boldsymbol{\lambda}$.

The overall procedure of the thermal surrogate modeling is summarized as Fig. 3. We direct interested readers to Ref. [5] for detailed derivations and procedure.

3.4.2 Surrogate Modeling of Microstructure Statistical Moments. In the grain growth model, there are three types of

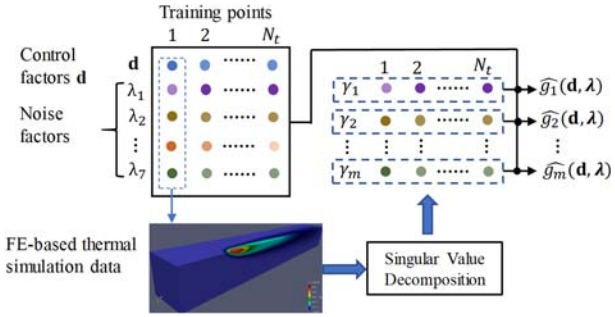

Fig. 3 Flowchart of surrogate modeling for the melt pool simulation model

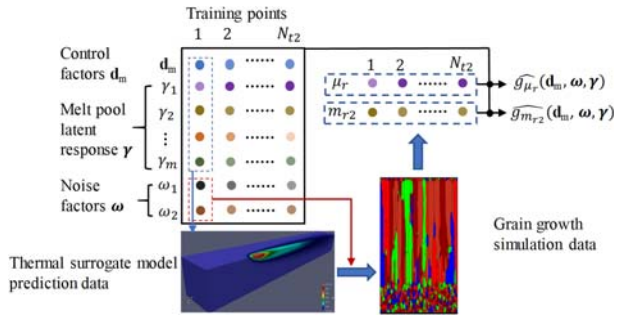

Fig. 4 Flowchart of surrogate modeling for the first-two statistical moments of the microstructure length/width ratio

variables: (1) the shared design variables (i.e., control factors) between the thermal model and the grain growth model that are denoted as $\mathbf{d}_m$, (2) the inputs from the thermal model which are the latent space responses $\boldsymbol{\gamma}$, and (3) the random variables (i.e., noise factors) $\boldsymbol{\omega}$ that belong to only the grain growth model. Figure 4 gives the overall flowchart of the grain growth surrogate modeling. In order to substitute the computationally expensive grain growth model with cheap data-driven surrogate models, we first generate N_{t2} training points for $\mathbf{d}_m$, $\boldsymbol{\gamma}$, and $\boldsymbol{\omega}$ (see Fig. 4).

For the ith training point, we first transform the latent space response $\gamma_1^{(i)}, \gamma_2^{(i)}, \ldots, \gamma_m^{(i)}$ into the original temperature field response as follows:

$$\hat{T}(i, \mathbf{s}) \approx \sum_{j=1}^{m} \gamma_j^{(i)} \boldsymbol{\eta}_j(\mathbf{s}), \quad \forall i = 1, 2, \ldots, N_{t2} \tag{20}$$

where $\hat{T}(i, \mathbf{s})$ is the temperature field response corresponding to ith training point. Note that the reconstructed temperature field may not fully satisfy the physics constraints in some regions due to the prediction errors. In that case, certain corrections to the temperature field need to be performed to make sure the physical laws are maintained. To avoid this burden, the temperature field responses obtained in Sec. 3.4.1 for melt pool surrogate modeling can be directly employed as training inputs for the grain growth surrogate modeling if $N_{t2} \leq N_t$.

Table 5 Pseudocode for the evaluation of the objective function using surrogate models

Step	Description
1	For given design variable $\mathbf{d}$ and $\mathbf{d}_m \subset \mathbf{d}$, generate random samples of $\boldsymbol{\lambda}$ and $\boldsymbol{\omega}$ and denote the generated samples as $\boldsymbol{\lambda}(i)$, $\boldsymbol{\omega}(i)$, $i = 1, 2, \ldots, n_{MCS}$ **For** $i = 1$ to n_{MCS}
2	Obtain the latent space responses $\gamma_j(i) = \hat{g}_j(\mathbf{d}, \boldsymbol{\lambda}(i))$, $j = 1, 2, \ldots, m$ using the latent space surrogate models (i.e., Eq. (18))
3	Obtain the prediction of μ_r using surrogate model $\mu_r(i) = \hat{g}_{\mu_r}(\mathbf{d}_m, \boldsymbol{\omega}(i), \boldsymbol{\gamma}(i))$, where $\boldsymbol{\gamma}(i) = [\gamma_1(i), \gamma_2(i), \ldots, \gamma_m(i)]$
4	Obtain the prediction of μ_r using surrogate model $m_{r2}(i) = \hat{g}_{m_{r2}}(\mathbf{d}_m, \boldsymbol{\omega}(i), \boldsymbol{\gamma}(i))$, where $\boldsymbol{\gamma}(i) = [\gamma_1(i), \gamma_2(i), \ldots, \gamma_m(i)]$ **End**
5	Compute the unconditional mean as $\mu_r(\mathbf{d}) = \frac{1}{n_{MCS}} \sum_{i=1}^{n_{MCS}} \mu_r(i)$ and unconditional second-order moment as $m_{r2} = \frac{1}{n_{MCS}} \sum_{i=1}^{n_{MCS}} m_{r2}(i)$
6	Compute $\sigma_r^2(\mathbf{d})$ using Eq. (14) and obtain the objective function evaluation

With the input temperature field $\hat{T}(i, \mathbf{s})$ and the training point $\mathbf{d}_m^{(i)}$ and $\boldsymbol{\omega}^{(i)}$, we then perform grain growth simulation and obtain corresponding microstructure statistical moments $\mu_r^{(i)}$ and $m_{r2}^{(i)}$. Based on the responses of $\mu_r^{(i)}$ and $m_{r2}^{(i)}$, $i = 1, 2, \ldots, N_{t2}$, we construct surrogate models for μ_r and m_{r2} as follows

$$\mu_r = \hat{g}_{\mu_r}(\mathbf{d}_m, \boldsymbol{\omega}, \boldsymbol{\gamma}) \tag{21}$$

$$m_{r2} = \hat{g}_{m_{r2}}(\mathbf{d}_m, \boldsymbol{\omega}, \boldsymbol{\gamma}) \tag{22}$$

where $\hat{g}_{\mu_r}(\cdot)$ and $\hat{g}_{m_{r2}}(\cdot)$ are the Kriging surrogate models.

Next, we discuss how to solve the robust design optimization model given in Eq. (16) based on the above surrogate models.

3.5 Solution of the Optimization Model After the Surrogate Modeling. In conclusion, the above surrogate modelings would basically construct target quantities (i.e., steady $\boldsymbol{T}(\boldsymbol{x})$, μ_r, and m_{r2}) as functions of control factors and respectively associated noise factors. This enables quick predictions of these quantities at any given point and thus efficient evaluation of the objective function for the robust process parameter optimization under uncertainty. Table 5 presents the pseudocode for the evaluation of the objective function after the construction of the surrogate models. There are mainly six steps. After we are able to efficiently evaluate the objective function for given points, we optimize the control factors or design variables by solving the optimization model given in Eq. (16). In this paper, the efficient global optimization method with noise data [74,75] is employed to solve the optimization model.

4 Results and Discussion

4.1 Physical Simulation and Validation. A sound physical model serves as the basis of correct uncertainty quantification and management. Validation of the current multiscale model is made step-by-step, i.e., in terms of both the FE thermal model and grain growth model.

4.1.1 Finite-Element-Based Thermal Simulation. Figure 5 shows previous experimentally validated pool predictions [49] and pool predictions using the current FE thermal model. Here, we selectively compare pools developed in the extreme cases of $I = 6$ mA ($v = 0.188$ m/s, $U = 60$ kV) and $I = 12$ mA ($v = 0.608$ m/s, $U = 60$ kV). It can be found that the pool shape informed by temperature field predicted agrees well with previous predictions. Specifically, measurements show that pools with the dimensions of $L = 2.25$ mm, $W = 0.70$ mm, $D = 0.30$ mm and $L = 3.97$ mm, $W = 0.68$ mm, $D = 0.23$ mm are, respectively, developed

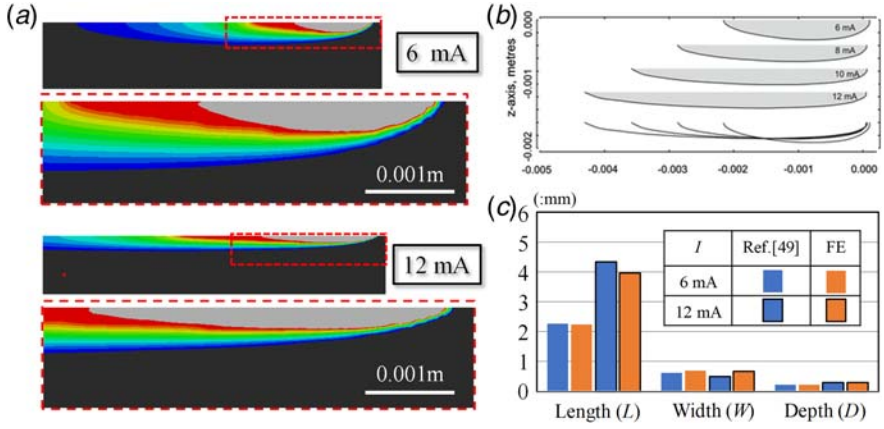

Fig. 5 Comparison of pool predictions between (*a*) the current FE thermal model and (*b*) previous experimentally validated model [49] and (*c*) quantitative comparison in terms of pool dimensions

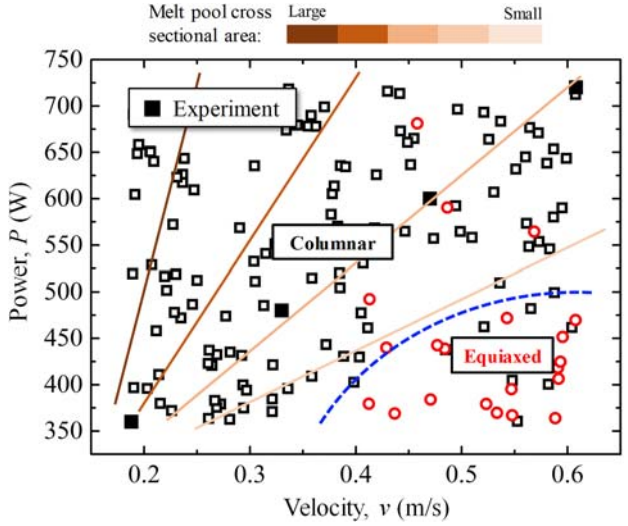

Fig. 6 Columnar-to-equiaxed structure transition *P–v* map. (Note that, the data scattering, e.g., the few columnar points observed in the equiaxed region, should not be mistaken as prediction errors. Instead, it just reflects the variability in the material's microstructure due to various uncertainty sources present during the AM process.) Previous experiment data [49] are also plotted. The constant pool area lines are just estimated based on Ref. [53], for a simple illustration of pool area variation in the *P–v* space.

under $I = 6$ mA and $I = 12$ mA, which also matches closely with previous results from a quantitative viewpoint.

4.1.2 Grain Growth Phase-field Simulation. Figure 6 shows columnar-to-equiaxed structure transition *P–v* map through performing extensive grain growth simulations. It is built just by taking advantage of the 150 grain growth simulations for generating training data. A columnar-to-equiaxed transition boundary (the dashed curve in Fig. 6) can be clearly delineated, although data scattering presents, e.g., columnar points occasionally observed in the equiaxed region. (Note that the data scattering should not be mistaken as prediction errors. It happens due to various uncertain factors considered and thus uncertainty in the final material's microstructure in current simulations.) The columnar/equiaxed delineation in Fig. 6 suggests a small-equiaxed region in the space of low power and high velocity. This is consistent with the previous experimental observation of finer grains with increasing beam speed [76], as well as the indication of the classical nucleation criteria [50]. That is, in this *P–v* space, correspondingly low-thermal gradient and high solidification rate tend to be developed, thus facilitating grain nucleation and equiaxed grain structure formation as indicated by the classical nucleation criteria. The experimentally observed columnar structures in Ref. [49] are also successfully located within the as-predicted columnar region. However, a fully equiaxed structure that is widely theoretically predicted is still rarely found in experiments as of now. The current *P–v* map may provide partial explanation for this, since in practice, the EBM machine in automatic mode would adopt certain speed functions [77] (namely, specific built-in power-velocity combinations instead of arbitrary user-defined ones) to maintain constant and appropriate melt pool cross-sectional area (the largest pool area perpendicular to the travel velocity direction). According to the constant pool area *P–v* map [53], these specific power–velocity combinations would usually be away from the equiaxed region to guarantee a sufficiently large pool area. Therefore, besides direct comparisons with experimental results, the ability to explain the gap between previous theoretical and experimental findings further justifies the *P–v* map, thus basically validating the microstructure prediction of the adopted grain growth model.

4.2 Surrogate Model Building and Cross-Validation. To train a surrogate model, we have run 280 thermal simulations and 150 grain growth simulations at specific training points (each training point or case corresponding to a specific combination of noise and control factors, as illustrated in Figs. 3 and 4). Of whom, the last 20 temperature profile data and 5 microstructure data are set aside for cross-validation; the remainder is training dataset.

4.2.1 Thermal Surrogate Model. Figure 7 shows partial cross-validation results of the thermal surrogate model. High-temperature fields resembling teardrops of different size are developed under different [**d**, λ]. By comparing Figs. 7(*a*) and 7(*b*), we find that the thermal surrogate model can predict similar temperature field development as the physical model under various conditions. However, running a single FE simulation usually requires about 50 min (based on Xeon CPU E5-2660), while a surrogate model just takes a couple of seconds for each prediction. Figure 7(*c*) shows that relatively large prediction errors mainly occur near the electron beam focus. This fact, however, affects little on employing thermal surrogate model for following grain growth simulations, since grain evolution cares only about the temperature field bounded by $T = T_{\beta\text{-}transus}$ and $T = T_{liquidus}$, which is exactly away from the superheated zone near EB focus. The same happens in the other 15 cross-validation results, which are thus not shown here due to the figure size limit. Therefore, in this study, the thermal surrogate model can be an effective substitute for the computationally costly FE-based thermal model.

4.2.2 Microstructure Surrogate Model. Grain evolution simulation and microstructure data generation are then greatly facilitated, by using the established thermal surrogate model to quickly know the high-temperature field that governs grain evolution. Figure 8 shows the cross-validation results of the trained microstructure prediction surrogate model. The comparison shows that the surrogate model successfully captures the grain structure variation (in terms of the mean and second moment of grain length/width ratio) with varying [**d**, θ]. In part, the acceptable error can be explained by the fact that the grain evolution is inherently a complex process that includes some probabilistic phenomenon. The structure prediction based on the grain evolution simulation would thus show a little random and stochastic characteristics, while the surrogate model prediction is deterministic.

4.3 Robust Design and Sensitivity Analysis. Robust design is now readily made with the cheap surrogate models. The design intervals are, respectively, $[T_{pre,L}, T_{pre,U}] = [923\text{ K}, 1003\text{ K}]$, $[P_L, P_U] = [360\text{ W}, 720\text{ W}]$, and $[v_L, v_U] = [0.188\text{ m/s}, 0.608\text{ m/s}]$ for the preheating temperature, EB power, and scanning speed, based on the accessible manufacturing condition in practice [18,49]. By solving the objective function Eq. (7), the optimal operating condition is found to be $T_{pre} = 946$ K, $P = 360$ W, and $v = 0.42$ m/s. It indicates that equiaxed grain structures could be certainly obtained even with various uncertainty sources, by using a low preheating temperature, low laser power, and intermediate scanning speed. The main reason is the introduction of a large number of new grains and highest survival of them under this manufacturing condition, thus greatly interrupting the original columnar grain growth. To be specific, low-thermal gradient G that encourages grain nucleation tend to be formed under a low preheating temperature and low laser power. On the other hand, an intermediate scanning speed could result in sufficiently high solidification rate R that allows grain nucleation, at the same time, without causing too much re-melting of new grains in previous layers. A too large speed, in contrary, would usually lead to a small melt pool accompanying with a shallow nucleation layer, thus making equiaxed structure formation vulnerable to uncertainty effects. In conclusion, consistently obtaining equiaxed grain structures during layer-by-layer AM process requires a delicate balance between different process parameters, which not only ensures sufficient grain nucleation but

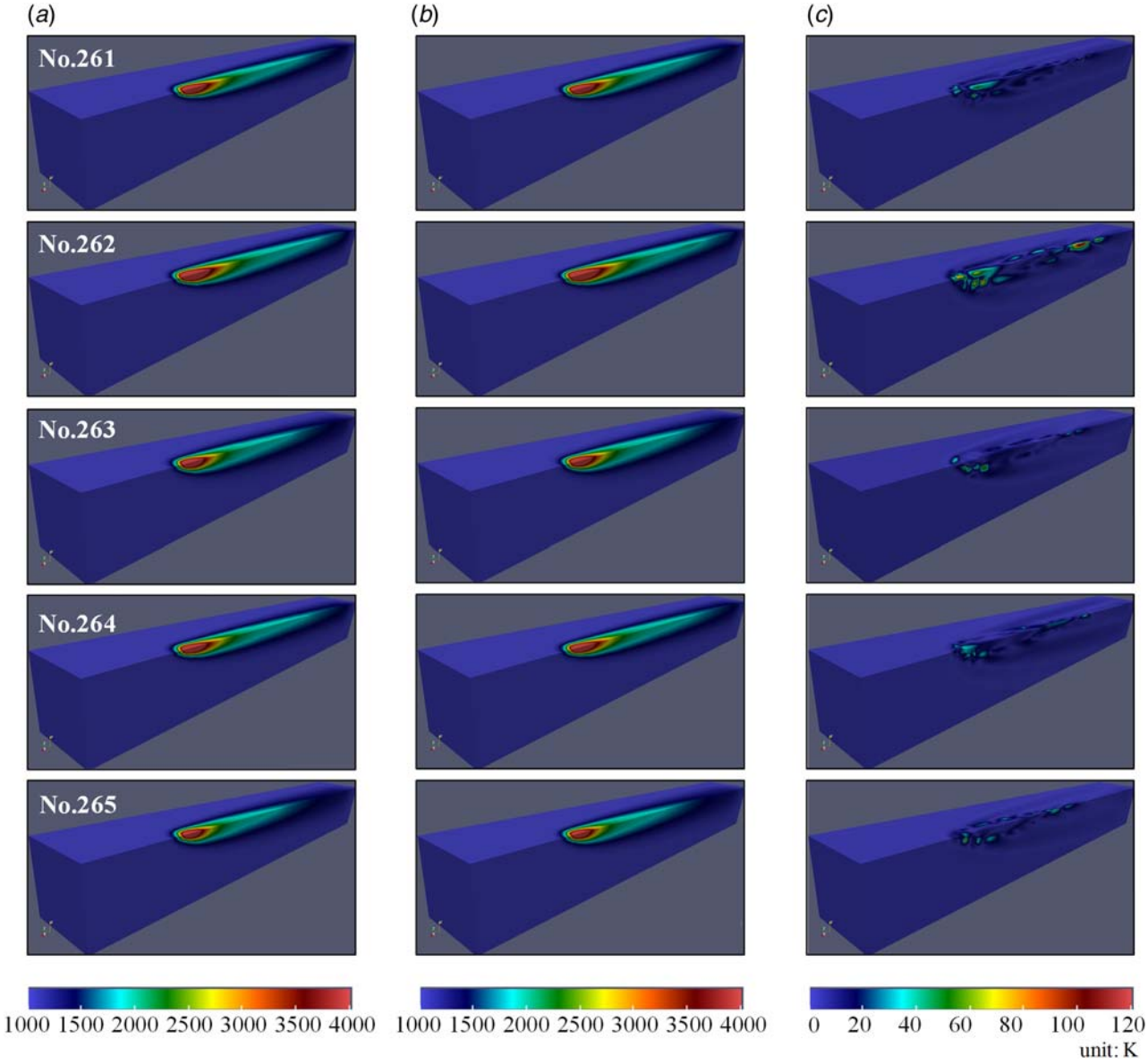

Fig. 7 Predictions of the steady temperature field developed as a function of control and noise factors [d, λ] by using the (*a*) finite-element-based thermal model and (*b*) thermal surrogate model. (*c*) Absolute errors of surrogate model predictions compared with finite-element simulations. (Here, each case or training point corresponds to a specific combination of control and noise factors [d, λ], see Sec. 3.4.).

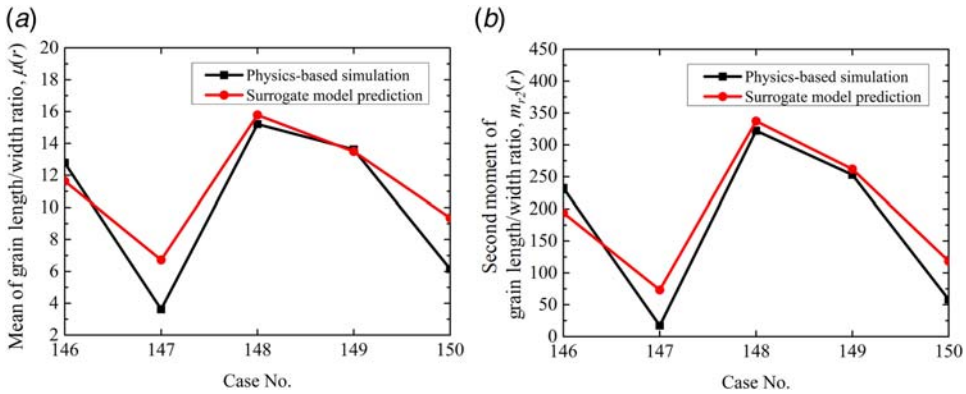

Fig. 8 Prediction of the grain length/width ratio distribution as a function of control and noise factors [d, θ], by using the physics-based AM simulation model and microstructure surrogate model: (*a*) mean of grain length/width ratio, $\mu(r)$ and (*b*) second moment of grain length/width ratio, $m_{r2}(r)$. (Here each case or training point corresponds to a specific combination of control and noise factors, [d, θ], see Sec. 3.4.).

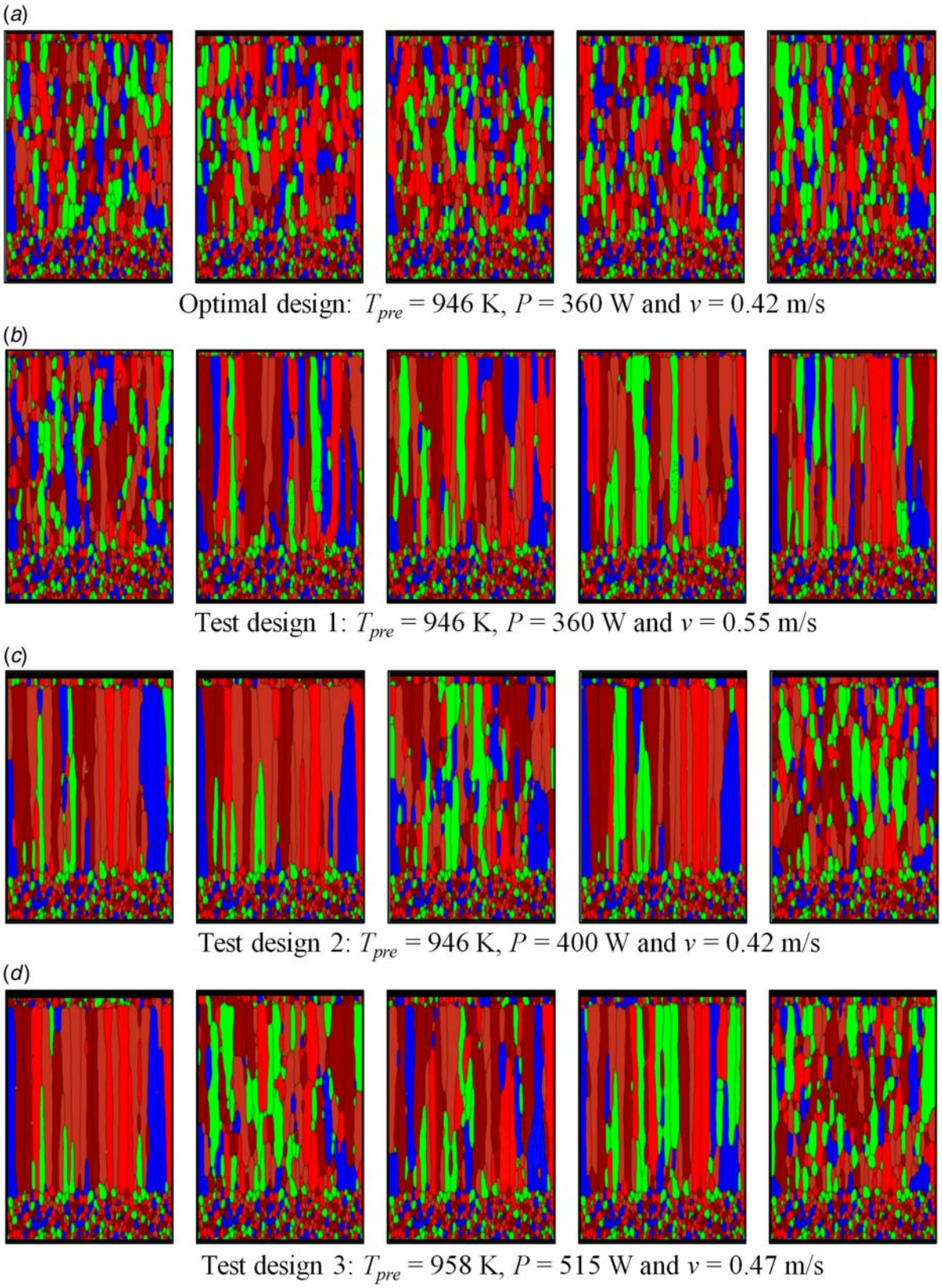

Fig. 9 Grain structure developments on the optimal manufacturing condition (robust design point) and test manufacturing conditions under uncertainty

also guarantees their high survival from re-melting and competitive growth against existing grains.

To verify the robust design result, 20 physical simulations with random noise factors were performed at the robust design point. First five simulation results are shown in Fig. 9(*a*). Equiaxed grain structures are indeed constantly produced under the optimal manufacturing condition obtained, although they show some difference due to the presence of noise factors or uncertainty sources. For further verification, we have also performed physical simulations at other three test points. Test point 1 is generated by increasing the

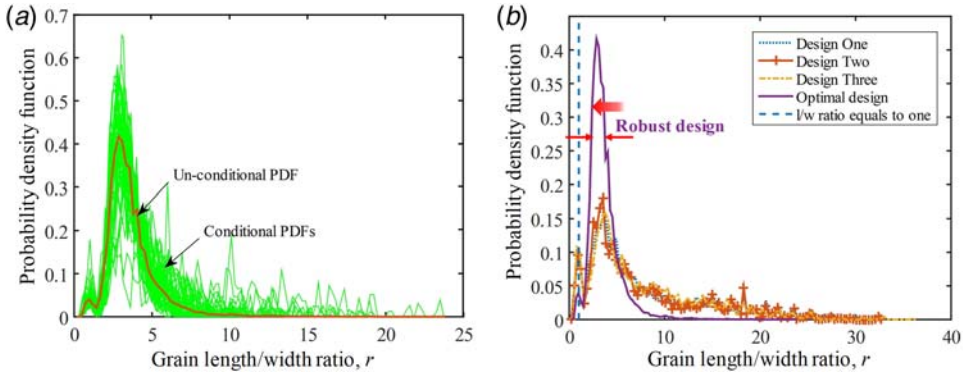

Fig. 10 (*a*) Grain length/width ratio distribution in terms of 20 different grain structures developed under the optimal manufacturing condition. They are summarized into one unconditional PDF distribution curve (the thick line), so as to better characterize the grain structure development with uncertainty. (*b*) Grain length/width ratio distribution (unconditional PDF) for different manufacturing conditions.

EB speed a little based on the robust design point, test point 2 is generated by increasing the EB power a little, and test point 3 is an arbitrary point. Grain structures developed under those conditions are also shown in Figs. 9(*b*)–9(*d*). It is found that the grain structure changes greatly under noises in all three test cases. Meantime, columnar grain structures are usually formed at all test points although small grains can be observed occasionally. To present all simulation results and for better comparison, we have collected the length/width ratio data in terms of all 20 grain structures for different manufacturing conditions, as plotted in Fig. 10. It is clearly shown that, through the robust design, the variation of grain structure, i.e., the width of r distribution, is greatly narrowed in comparison with the other three. Furthermore, the robust design tends to push the r distribution to approach $r = 1$ line (the perfectly equiaxed grain structure). It is thus proved that the robust design point obtained represents the optimal manufacturing condition as compared with probably any of others. The precise obtainment of the robust manufacturing condition, again, demonstrates the capability of the surrogate model in accurately capturing complex relationships between target quantities and process parameters as well as noise factors, besides the crossvalidation made earlier.

The global sensitivity analysis [78] is also made to reveal the contribution of different uncertainty sources to the variation of materials microstructure. Figure 11 indicates that the mean of grain length/width ratio is most sensitive to density and grain boundary energy, while the variation of grain length/width ratio shows the highest sensitivity to specific heat capacity and grain growth activation energy. Thus, reducing the noise level of density and grain boundary energy could make it more likely to obtain equiaxed grain structures under uncertainty and reducing the noise level of specific heat capacity and grain growth activation energy would help minimize the grain structure variation among products. Note that, global sensitivity analysis results will be affected by the random distributions and distribution parameters of uncertainty sources. Collecting more data to model the uncertainty sources could further improve uncertainty quantification and sensitivity analysis.

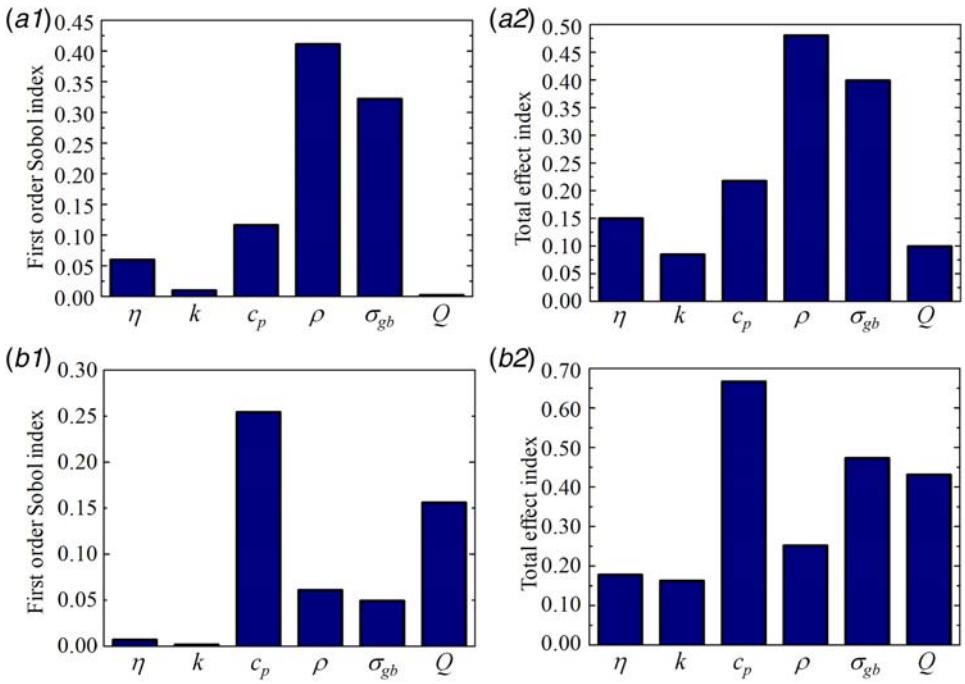

Fig. 11 (*a*) Sensitivity of mean of length/width ratio to various noise factors and (*b*) sensitivity of the variance of length/width ratio to various noise factors

4.4 Discussion. In recent years, data-driven approaches (e.g., machine learning and statistical learning based) have appeared frequently in the engineering field as powerful data analysis and predictive modeling tools [79–83]. However, their application in the AM study is still rare, if any, with the main function as a simple data fitting tool in terms of low-dimensional inputs and outputs [84,85]. The current study, to authors' best knowledge, presents one of the first efforts to perform multilevel uncertainty quantification and management for metal-based AM process, with the aid of advanced application of the data-driven technique.

4.4.1 Level-by-Level Surrogate Model Building. A special feature of the current approach is its level-by-level surrogate model building manner. This brings about several advantages compared with directly treating all connected levels as a single black box. First, by level-by-level surrogate model building, validation of corresponding models is also made at each level. Hence, incorrect UQ and UM resulting essentially from large prediction errors of either physical or surrogate models at any level can be found easily. Also, benefiting from its modular feature, the individual surrogate model established can be potentially linked to other AM models (either lower or higher levels), thus enabling faster creation of a different multilevel UQ model in future studies. This helps ultimately construct the full network for uncertainty aggregation in the AM process [11]. For example, the established thermal surrogate model can be connected to the lower-level heat source model [59] and/or higher-level lack-of-fusion porosity predictive model [86]. Another advantage offered is that some noise factors showing little uncertainty propagation could be suspected early from a UQ at lower levels. By eliminating them, the whole UQ procedure would require less physics-based simulations with reduced inputs than a one-step multilevel UQ. This especially alleviates the computational burden for a multilevel UQ that abounds with numerous uncertainty sources from different levels.

4.4.2 Process Optimization and Future Applications. Process parameters optimization, usually with the aim of controlling local thermal conditions to enhance grain nucleation [53,54,87], is an effective way to tailor materials microstructure and achieve quality improvement. It requires no additional efforts and costs as compared with, for example, combining rolling deformation [2,88] or adding inoculating particles [70] to tailor grain structure. The conventional process optimization, however, may yield optimal manufacturing condition that leads to unexpected product quality (e.g., columnar microstructure), due to the existence of various uncertainty sources in practice. The data-driven approach presented in this study allows advanced optimization of processing parameters under uncertainty, thus guaranteeing the repetitive production of high-quality products. It has demonstrated the data-driven technique, with training data acquired at an acceptable number of training points, can well capture the complicate relationship between AM process parameters and target quantities or even the high-dimensional temperature field. This strongly suggests the possibility of facilitating other types of complicate AM process optimization, like robust design in terms of porosity control or direct mechanical property control, by using a similar data-driven approach.

4.4.3 Limitation of the Current Study. Finally, we would like to emphasize that the quantity of interest in this study is materials microstructure. Process optimization is made aiming primarily to improve the microstructure to enhance product quality; other quality metrics such as the porosity level have not been accounted for in this research. In this case, the optimal manufacturing condition mainly for obtaining good microstructures may cause other problems, such as insufficient pool overlapping and thus lack-of-fusion porosity [89]. Therefore, this research just selects the material's microstructure as an exemplar target quantity, to bring out the capability of the data-driven technique in facilitating complicate AM process optimizations. Nonetheless, the current approach can be readily extended to, for instance, the process optimization in terms of controlling simultaneously the microstructure and porosity with reasonable modification, like by further coupling the as-mentioned porosity predictive model. In fact, there are various AM simulation models that enable the connecting process to even more quality metrics, such as surface structure [90], residual stress [91,92], and dimensional accuracy [93]. In this regard, based on the data-driven approach, efficient multiobjective optimization could be carried out for a comprehensive control of product quality in the near future.

5 Conclusion

This paper presents a data-driven AM process optimization approach, backboned by an advanced multiscale multiphysics AM simulation model and Kriging surrogate model. Based on this approach, multilevel uncertainty quantification and management are successfully performed with respect to the EBM of Ti-6Al-4V. Concluding remarks are made as below:

- The two-level surrogate model, which is trained with simulation-obtained data at an acceptable computational cost, i.e., 280 thermal simulations and 150 grain growth phase-field simulations with a total computation time of about 2 weeks, achieves high accuracy in predicting temperature profile and materials microstructure.
- With the established surrogate models, uncertainty quantification analysis is readily conducted, revealing the highest sensitivity of materials microstructure variation to specific heat capacity and grain growth activation energy.
- Control factors, here AM process parameters, are optimized through robust design. The optimal combination of process parameters, i.e., a low preheating temperature, low laser power, and intermediate scanning speed, is suggested to guarantee fabricating products with consistently equiaxed grain structures. This specific processing condition not only ensures sufficient nucleation of new grains but also guarantees their high survival from re-melting and competitive growth against existing grains.
- The first attempt made by this study, i.e., multilevel uncertainty quantification and management in AM process through the cooperation of the advanced multiscale AM simulation and surrogate modeling technique demonstrates the great potential of the data-driven technique to facilitate AM process optimization in terms of different product qualities of interest in future studies.

Acknowledgment

This research was supported by the program of ORAU Ralph E. Powe Junior Faculty Enhancement Award and National Science Foundation under grant CMMI-1662854. P.W. Liu and X.Y. Cui thank the Foundation for Innovative Research Groups of the National Natural Science Foundation of China, China (51621004), and China Scholarship Council. The computer simulations were carried out on the clusters of High Performance Computing Collaboratory (HPC^2) at Mississippi State University.

References

[1] Brandl, E., Schoberth, A., and Leyens, C., 2012, "Morphology, Microstructure, and Hardness of Titanium (Ti-6Al-4V) Blocks Deposited by Wire-Feed Additive Layer Manufacturing (ALM)," Mater. Sci. Eng. A, **532**(Suppl. C), pp. 295–307.
[2] Donoghue, J., Antonysamy, A., Martina, F., Colegrove, P., Williams, S., and Prangnell, P., 2016, "The Effectiveness of Combining Rolling Deformation With Wire–Arc Additive Manufacture on β-Grain Refinement and Texture Modification in Ti–6Al–4V," Mater. Charact., **114**, pp. 103–114.
[3] Körner, C., 2016, "Additive Manufacturing of Metallic Components by Selective Electron Beam Melting—A Review," Int. Mater. Rev., **61**(5), pp. 361–377.
[4] Laureijs, R. E., Roca, J. B., Narra, S. P., Montgomery, C., Beuth, J. L., and Fuchs, E. R., 2017, "Metal Additive Manufacturing: Cost Competitive Beyond Low Volumes," ASME J. Manuf. Sci. Eng., **139**(8), p. 081010.

[5] Nath, P., Hu, Z., and Mahadevan, S., 2017, "Multi-Level Uncertainty Quantification in Additive Manufacturing," Solid Freeform Fabrication: Proceedings of the 28th Annual International Solid Freeform Fabrication Symposium, Austin, TX, Aug. 7–9, Univeristy of Texas at Austin, Austin, TX, pp. 7–9.
[6] Ma, L., Fong, J., Lane, B., Moylan, S., Filliben, J., Heckert, A., and Levine, L., 2015, "Using Design of Experiments in Finite Element Modeling to Identify Critical Variables for Laser Powder Bed Fusion," International Solid Freeform Fabrication Symposium, Austin, TX, Aug. 10–12, Univeristy of Texas at Austin, Austin, TX, pp. 219–228.
[7] Chen, W., Allen, J. K., Tsui, K.-L., and Mistree, F., 1996, "A Procedure for Robust Design: Minimizing Variations Caused by Noise Factors and Control Factors," ASME J. Mech. Des., **118**(4), pp. 478–485.
[8] Chan, S., and Elsheikh, A. H., 2018, "A Machine Learning Approach for Efficient Uncertainty Quantification Using Multiscale Methods," J. Comput. Phys., **354**, pp. 493–511.
[9] Zhu, Y., and Zabaras, N., 2018, "Bayesian Deep Convolutional Encoder–Decoder Networks for Surrogate Modeling and Uncertainty Quantification," J. Comput. Phys., **366**, pp. 415–447.
[10] Sankararaman, S., Ling, Y., and Mahadevan, S., 2011, "Uncertainty Quantification and Model Validation of Fatigue Crack Growth Prediction," Eng. Fract. Mech., **78**(7), pp. 1487–1504.
[11] Hu, Z., and Mahadevan, S., 2017, "Uncertainty Quantification and Management in Additive Manufacturing: Current Status, Needs, and Opportunities," Int. J. Adv. Manuf. Technol., **93**(5–8), pp. 2855–2874.
[12] Kamath, C., 2016, "Data Mining and Statistical Inference in Selective Laser Melting," Int. J. Adv. Manuf. Technol., **86**(5–8), pp. 1659–1677.
[13] Lopez, F., Witherell, P., and Lane, B., 2016, "Identifying Uncertainty in Laser Powder Bed Fusion Additive Manufacturing Models," ASME J. Mech. Des., **138**(11), p. 114502.
[14] Haines, M., Plotkowski, A., Frederick, C. L., Schwalbach, E. J., and Babu, S. S., 2018, "A Sensitivity Analysis of the Columnar-to-Equiaxed Transition for Ni-Based Superalloys in Electron Beam Additive Manufacturing," Comput. Mater. Sci., **155**, pp. 340–349.
[15] Moser, D., Fish, S., Beaman, J., and Murthy, J., 2014, "Multi-Layer Computational Modeling of Selective Laser Sintering Processes," ASME 2014 International Mechanical Engineering Congress and Exposition, Montreal, Canada, Nov. 14–20, p. V02AT02A008.
[16] Tapia, G., King, W., Johnson, L., Arroyave, R., Karaman, I., and Elwany, A., 2018, "Uncertainty Propagation Analysis of Computational Models in Laser Powder Bed Fusion Additive Manufacturing Using Polynomial Chaos Expansions," ASME J. Manuf. Sci. Eng., **140**(12), p. 121006.
[17] Fallah, V., Amoorezaei, M., Provatas, N., Corbin, S. F., and Khajepour, A., 2012, "Phase-Field Simulation of Solidification Morphology in Laser Powder Deposition of Ti–Nb Alloys," Acta Mater., **60**(4), pp. 1633–1646.
[18] Sahoo, S., and Chou, K., 2016, "Phase-Field Simulation of Microstructure Evolution of Ti–6Al–4V in Electron Beam Additive Manufacturing Process," Addit. Manuf., **9**, pp. 14–24.
[19] Acharya, R., Sharon, J. A., and Staroselsky, A., 2017, "Prediction of Microstructure in Laser Powder Bed Fusion Process," Acta Mater., **124**, pp. 360–371.
[20] Raghavan, N., Dehoff, R., Pannala, S., Simunovic, S., Kirka, M., Turner, J., Carlson, N., and Babu, S. S., 2016, "Numerical Modeling of Heat-Transfer and the Influence of Process Parameters on Tailoring the Grain Morphology of IN718 in Electron Beam Additive Manufacturing," Acta Mater., **112**, pp. 303–314.
[21] Gäumann, M., Bezencon, C., Canalis, P., and Kurz, W., 2001, "Single-Crystal Laser Deposition of Superalloys: Processing–Microstructure Maps," Acta Mater., **49**(6), pp. 1051–1062.
[22] Hunt, J., 1984, "Steady State Columnar and Equiaxed Growth of Dendrites and Eutectic," Mater. Sci. Eng., **65**(1), pp. 75–83.
[23] Gockel, J., Beuth, J., and Taminger, K., 2014, "Integrated Control of Solidification Microstructure and Melt Pool Dimensions in Electron Beam Wire Feed Additive Manufacturing of Ti-6Al-4V," Addit. Manuf., **1**, pp. 119–126.
[24] Mani, M., Feng, S., Lane, B., Donmez, A., Moylan, S., and Fesperman, R., 2015, *Measurement Science Needs for Real-Time Control of Additive Manufacturing Powder bed Fusion Processes*, US Department of Commerce, National Institute of Standards and Technology. NISTIR 8036.
[25] Liu, P., Ji, Y., Wang, Z., Qiu, C., Antonysamy, A., Chen, L.-Q., Cui, X., and Chen, L., 2018, "Investigation on Evolution Mechanisms of Site-Specific Grain Structures During Metal Additive Manufacturing," J. Mater. Process. Technol., **257**, pp. 191–202.
[26] Liu, P., Cui, X., Deng, J., Li, S., Li, Z., and Chen, L., 2019, "Investigation of Thermal Responses During Metallic Additive Manufacturing Using a 'Tri-Prism' Finite Element Method," Int. J. Therm. Sci., **136**, pp. 217–229.
[27] Liu, P., Wang, Z., Xiao, Y., Mark, H. F., Cui, X., and Chen, L., 2019, "Insight into the Mechanisms of Columnar to Equiaxed Grain Transition During Metallic Additive Manufacturing," Addit. Manuf., **26**, pp. 22–29.
[28] Donoghue, J., Gholinia, A., Fonseca, J. Q. d., and Prangnell, P., 2015, "In-Situ High Temperature EBSD Analysis of the Effect of a Deformation Step on the Alpha to Beta Transition in Additive Manufactured Ti-6Al-4V," Proceedings of the 13th World Conference on Titanium, San Diego, CA, Aug. 16–20, The Minerals, Metals and Materials Society, Warrendale, PA, pp. 1283–1288.
[29] Antonysamy, A. A., Meyer, J., and Prangnell, P., 2013, "Effect of Build Geometry on the β-Grain Structure and Texture in Additive Manufacture of Ti 6Al 4V by Selective Electron Beam Melting," Mater. Charact., **84**, pp. 153–168.
[30] Gockel, J., Klingbeil, N., and Bontha, S., 2016, "A Closed-Form Solution for the Effect of Free Edges on Melt Pool Geometry and Solidification Microstructure in Additive Manufacturing of Thin-Wall Geometries," Metall. Mater. Trans. B, **47**(2), pp. 1400–1408.
[31] Kundin, J., Mushongera, L., and Emmerich, H., 2015, "Phase-Field Modeling of Microstructure Formation During Rapid Solidification in Inconel 718 Superalloy," Acta Mater., **95**, pp. 343–356.
[32] Li, J., Wang, Q., and Michaleris, P. P., 2018, "An Analytical Computation of Temperature Field Evolved in Directed Energy Deposition," ASME J. Manuf. Sci. Eng., **140**(10), p. 101004.
[33] Rosenthal, D., 1946, "The Theory of Moving Sources of Heat and Its Application of Metal Treatments," Trans. ASME, **68**, pp. 849–866.
[34] Nie, P., Ojo, O., and Li, Z., 2014, "Numerical Modeling of Microstructure Evolution During Laser Additive Manufacturing of a Nickel-Based Superalloy," Acta Mater., **77**, pp. 85–95.
[35] Cheng, B., Price, S., Lydon, J., Cooper, K., and Chou, K., 2014, "On Process Temperature in Powder-Bed Electron Beam Additive Manufacturing: Model Development and Validation," ASME J. Manuf. Sci. Eng., **136**(6), p. 061018.
[36] Wei, L. C., Ehrlich, L. E., Powell-Palm, M. J., Montgomery, C., Beuth, J., and Malen, J. A., 2018, "Thermal Conductivity of Metal Powders for Powder Bed Additive Manufacturing," Addit. Manuf., **21**, pp. 201–208.
[37] Cheng, B., Lane, B., Whiting, J., and Chou, K., 2018, "A Combined Experimental-Numerical Method to Evaluate Powder Thermal Properties in Laser Powder Bed Fusion," ASME J. Manuf. Sci. Eng., **140**(11), p. 111008.
[38] Ghosh, S., Ma, L., Ofori-Opoku, N., and Guyer, J. E., 2017, "On the Primary Spacing and Microsegregation of Cellular Dendrites in Laser Deposited Ni–Nb Alloys," Modell. Simul. Mater. Sci. Eng., **25**(6), p. 065002.
[39] ABAQUS version 6.10, 2010, "User Subroutines Reference Manual." Dassault Systemes Simulia Corp.
[40] Price, S., Lydon, J., Cooper, K., and Chou, K., 2013, "Experimental Temperature Analysis of Powder-Based Electron Beam Additive Manufacturing," Proceedings of the Solid Freeform Fabrication Symposium, Austin, TX, Aug. 12–14, Univeristy of Texas at Austin, Austin, TX, pp. 162–173.
[41] Wang, X., Liu, P., Ji, Y., Liu, Y., Horstemeyer, M., and Chen, L., 2019, "Investigation on Microsegregation of IN718 Alloy During Additive Manufacturing via Integrated Phase-Field and Finite-Element Modeling," J. Mater. Eng. Perform., **28**(2), pp. 657–665.
[42] Rai, A., Markl, M., and Körner, C., 2016, "A Coupled Cellular Automaton–Lattice Boltzmann Model for Grain Structure Simulation During Additive Manufacturing," Comput. Mater. Sci., **124**, pp. 37–48.
[43] Rodgers, T. M., Madison, J. D., and Tikare, V., 2017, "Simulation of Metal Additive Manufacturing Microstructures Using Kinetic Monte Carlo," Comput. Mater. Sci., **135**, pp. 78–89.
[44] Baykasoglu, C., Akyildiz, O., Candemir, D., Yang, Q., and To, A. C., 2018, "Predicting Microstructure Evolution During Directed Energy Deposition Additive Manufacturing of Ti-6Al-4V," ASME J. Manuf. Sci. Eng., **140**(5), p. 051003.
[45] Krill, C. E. III, and Chen, L.-Q., 2002, "Computer Simulation of 3-D Grain Growth Using a Phase-Field Model," Acta Mater., **50**, pp. 3057–3073.
[46] Lee, D. N., Kim, K.-h., Lee, Y.-g., and Choi, C.-H., 1997, "Factors Determining Crystal Orientation of Dendritic Growth During Solidification," Mater. Chem. Phys., **47**(2), pp. 154–158.
[47] Ohno, M., Yamaguchi, T., Sato, D., and Matsuura, K., 2013, "Existence or Nonexistence of Thermal Pinning Effect in Grain Growth Under Temperature Gradient," Comput. Mater. Sci., **69**, pp. 7–13.
[48] Ataibis, V., and Taktak, S., 2015, "Characteristics and Growth Kinetics of Plasma Paste Borided Cp–Ti and Ti6Al4V Alloy," Surf. Coat. Technol., **279**, pp. 65–71.
[49] Al-Bermani, S., Blackmore, M., Zhang, W., and Todd, I., 2010, "The Origin of Microstructural Diversity, Texture, and Mechanical Properties in Electron Beam Melted Ti-6Al-4V," Metall. Mater. Trans. A, **41**(13), pp. 3422–3434.
[50] Schempp, P., Cross, C., Pittner, A., Oder, G., Neumann, R. S., Rooch, H., Dörfel, I., Österle, W., and Rethmeier, M., 2014, "Solidification of GTA Aluminum Weld Metal: Part 1—Grain Morphology Dependent upon Alloy Composition and Grain Refiner Content," Weld. J., **93**(2), pp. 53s–59s.
[51] Schempp, P., Cross, C., Pittner, A., and Rethmeier, M., 2014, "Solidification of GTA Aluminum Weld Metal: Part 2—Thermal Conditions and Model for Columnar-to-Equiaxed Transition," Weld. J., **93**, pp. 69–77.
[52] Charbon, C., and Rappaz, M., 1993, "3D Probabilistic Modelling of Equiaxed Eutectic Solidification," Modell. Simul. Mater. Sci. Eng., **1**(4), p. 455.
[53] Gockel, J., and Beuth, J., 2013, "Understanding Ti-6Al-4V Microstructure Control in Additive Manufacturing Via Process Maps," Solid Freeform Fabrication Proceedings, Austin, TX, Aug. 12–14, University of Texas at Austin, Austin, TX, pp. 12–14.
[54] Kobryn, P. A., and Semiatin, S., 2003, "Microstructure and Texture Evolution During Solidification Processing of Ti–6Al–4V," J. Mater. Process. Technol., **135**(2), pp. 330–339.
[55] Sahoo, S., 2014, "Microstructure Simulation of Ti-6Al-4V Biomaterial Produced by Electron Beam Additive Manufacturing Process," Int. J. Nano Biomater., **5**(4), pp. 228–235.
[56] Boivineau, M., Cagran, C., Doytier, D., Eyraud, V., Nadal, M.-H., Wilthan, B., and Pottlacher, G., 2006, "Thermophysical Properties of Solid and Liquid Ti-6Al-4V (TA6V) Alloy," Int. J. Thermophys., **27**(2), pp. 507–529.
[57] Brooks, R. F., Robinson, J. A., Chapman, L. A., and Richardson, M. J., 2004, "The Enthalpy of a Solid and Liquid Titanium-Aluminium-Vanadium Alloy," High Temp.-High Press, **35**(2), pp. 193–198.
[58] Wu, L., and Zhang, J., 2018, "Phase Field Simulation of Dendritic Solidification of Ti-6Al-4V During Additive Manufacturing Process," JOM, **70**(10), pp. 2392–2399.

[59] Yan, W., Smith, J., Ge, W., Lin, F., and Liu, W. K., 2015, "Multiscale Modeling of Electron Beam and Substrate Interaction: A New Heat Source Model," Comput. Mech., **56**(2), pp. 265–276.
[60] Klassen, A., Bauereiß, A., and Körner, C., 2014, "Modelling of Electron Beam Absorption in Complex Geometries," J. Phys. D: Appl. Phys., **47**(6), p. 065307.
[61] Körner, C., Attar, E., and Heinl, P., 2011, "Mesoscopic Simulation of Selective Beam Melting Processes," J. Mater. Process. Technol., **211**(6), pp. 978–987.
[62] Hu, Z., and Mahadevan, S., 2017, "Uncertainty Quantification in Prediction of Material Properties During Additive Manufacturing," Scr. Mater., **135**, pp. 135–140.
[63] Xiao, Y., Zhan, H., Gu, Y., and Li, Q., 2017, "Modeling Heat Transfer During Friction Stir Welding Using a Meshless Particle Method," Int. J. Heat Mass Transf., **104**, pp. 288–300.
[64] Roth, T. A., and Suppayak, P., 1978, "The Surface and Grain Boundary Free Energies of Pure Titanium and the Titanium Alloy Ti-6AI-4V," Mater. Sci. Eng., **35**(2), pp. 187–196.
[65] Roth, T. A., and Henning, W. D., 1985, "The Surface and Grain Boundary Free Energies and the Self-Diffusion Coefficient of 5Al-2.5Sn Titanium Alloy," Mater. Sci. Eng., **76**, pp. 187–194.
[66] Gil, F., and Planell, J., 2000, "Behaviour of Normal Grain Growth Kinetics in Single Phase Titanium and Titanium Alloys," Mater. Sci. Eng. A, **283**(1), pp. 17–24.
[67] Ding, R., and Guo, Z. X., 2002, "Microstructural Modelling of Dynamic Recrystallisation Using an Extended Cellular Automaton Approach," Comput. Mater. Sci., **23**(1), pp. 209–218.
[68] Mishra, S., and DebRoy, T., 2004, "Measurements and Monte Carlo Simulation of Grain Growth in the Heat-Affected Zone of Ti–6Al–4V Welds," Acta Mater., **52**(5), pp. 1183–1192.
[69] Jamshidinia, M., Kong, F., and Kovacevic, R., 2013, "Numerical Modeling of Heat Distribution in the Electron Beam Melting® of Ti-6Al-4V," ASME J. Manuf. Sci. Eng., **135**(6), p. 061010.
[70] Martin, J. H., Yahata, B. D., Hundley, J. M., Mayer, J. A., Schaedler, T. A., and Pollock, T. M., 2017, "3D Printing of High-Strength Aluminium Alloys," Nature, **549**(7672), pp. 365–369.
[71] Hu, Z., and Mahadevan, S., 2016, "Global Sensitivity Analysis-Enhanced Surrogate (GSAS) Modeling for Reliability Analysis," Struct. Multidiscip. Optim., **53**(3), pp. 501–521.
[72] Helton, J. C., and Davis, F. J., 2003, "Latin Hypercube Sampling and the Propagation of Uncertainty in Analyses of Complex Systems," Reliab. Eng. Syst. Saf., **81**(1), pp. 23–69.
[73] Hu, Z., Ao, D., and Mahadevan, S., 2017, "Calibration Experimental Design Considering Field Response and Model Uncertainty," Comput. Methods Appl. Mech. Eng., **318**, pp. 92–119.
[74] Jones, D. R., Schonlau, M., and Welch, W. J., 1998, "Efficient Global Optimization of Expensive Black-Box Functions," J. Global Optim., **13**(4), pp. 455–492.
[75] Forrester, J., Keane, A. I., and Bressloff, A. J., and W, N., 2006, "Design and Analysis of 'Noisy' Computer Experiments," AIAA J., **44**(10), pp. 2331–2339.
[76] Gong, X., Lydon, J., Cooper, K., and Chou, K., 2014, "Beam Speed Effects on Ti–6Al–4V Microstructures in Electron Beam Additive Manufacturing," J. Mater. Res., **29**(17), pp. 1951–1959.
[77] Narra, S. P., Cunningham, R., Beuth, J., and Rollett, A. D., 2018, "Location Specific Solidification Microstructure Control in Electron Beam Melting of Ti-6Al-4V," Addit. Manuf., **19**, pp. 160–166.
[78] Hu, Z., and Mahadevan, S., 2018, "Probability Models for Data-Driven Global Sensitivity Analysis," Reliab. Eng. Syst. Saf., 187, pp. 40–57.
[79] Stanev, V., Oses, C., Kusne, A. G., Rodriguez, E., Paglione, J., Curtarolo, S., and Takeuchi, I., 2018, "Machine Learning Modeling of Superconducting Critical Temperature," npj Comput. Mater., **4**(1), p. 29.
[80] Jäger, M. O., Morooka, E. V., Canova, F. F., Himanen, L., and Foster, A. S., 2018, "Machine Learning Hydrogen Adsorption on Nanoclusters Through Structural Descriptors," npj Comput. Mater, **4**(1), p. 37.
[81] Rovinelli, A., Sangid, M. D., Proudhon, H., and Ludwig, W., 2018, "Using Machine Learning and a Data-Driven Approach to Identify the Small Fatigue Crack Driving Force in Polycrystalline Materials," npj Comput. Mater., **4**(1), p. 35.
[82] Ward, L., Agrawal, A., Choudhary, A., and Wolverton, C., 2016, "A General-Purpose Machine Learning Framework for Predicting Properties of Inorganic Materials," npj Comput. Mater., **2**, p. 16028.
[83] Medasani, B., Gamst, A., Ding, H., Chen, W., Persson, K. A., Asta, M., Canning, A., and Haranczyk, M., 2016, "Predicting Defect Behavior in B2 Intermetallics by Merging Ab Initio Modeling and Machine Learning," npj Comput. Mater, **2**(1), p. 1.
[84] Zhang, W., Mehta, A., Desai, P. S., and Fred Higgs, P. C., III, 2017, "Machine Learning Enabled Powder Spreading Process Map For Metal Additive Manufacturing (AM)," 2017 Solid Freeform Fabrication Symposium Proceedings, Austin, TX, Aug. 7–9, Univeristy of Texas at Austin, Austin, TX.
[85] Tapia, G., Khairallah, S., Matthews, M., King, W. E., and Elwany, A., 2018, "Gaussian Process-Based Surrogate Modeling Framework for Process Planning in Laser Powder-Bed Fusion Additive Manufacturing of 316L Stainless Steel," Int. J. Adv. Manuf. Technol., **94**(9–12), pp. 3591–3603.
[86] Tang, M., Pistorius, P. C., and Beuth, J. L., 2017, "Prediction of Lack-of-Fusion Porosity for Powder Bed Fusion," Addit. Manuf., **14**, pp. 39–48.
[87] Dehoff, R., Kirka, M., Sames, W., Bilheux, H., Tremsin, A., Lowe, L., and Babu, S., 2015, "Site Specific Control of Crystallographic Grain Orientation Through Electron Beam Additive Manufacturing," Mater. Sci. Technol., **31**(8), pp. 931–938.
[88] Colegrove, P. A., Martina, F., Roy, M. J., Szost, B. A., Terzi, S., Williams, S. W., Withers, P. J., and Jarvis, D., 2014, "High Pressure Interpass Rolling of Wire+ arc Additively Manufactured Titanium Components," Adv. Mater. Res., **996**, pp. 694–700.
[89] Teng, C., Gong, H., Szabo, A., Dilip, J., Ashby, K., Zhang, S., Patil, N., Pal, D., and Stucker, B., 2017, "Simulating Melt Pool Shape and Lack of Fusion Porosity for Selective Laser Melting of Cobalt Chromium Components," ASME J. Manuf. Sci. Eng., **139**(1), p. 011009.
[90] Qiu, C., Panwisawas, C., Ward, M., Basoalto, H. C., Brooks, J. W., and Attallah, M. M., 2015, "On the Role of Melt Flow Into the Surface Structure and Porosity Development During Selective Laser Melting," Acta Mater., **96**, pp. 72–79.
[91] Lu, X., Lin, X., Chiumenti, M., Cervera, M., Hu, Y., Ji, X., Ma, L., Yang, H., and Huang, W., 2019, "Residual Stress and Distortion of Rectangular and S-Shaped Ti-6Al-4V Parts by Directed Energy Deposition: Modelling and Experimental Calibration," Addit. Manuf. **26**, 166–179.
[92] Jayanath, S., and Achuthan, A., 2018, "A Computationally Efficient Finite Element Framework to Simulate Additive Manufacturing Processes," ASME J. Manuf. Sci. Eng., **140**(4), p. 041009.
[93] Lyu, J., and Manoochehri, S., 2018, "Modeling Machine Motion and Process Parameter Errors for Improving Dimensional Accuracy of Fused Deposition Modeling Machines," ASME J. Manuf. Sci. Eng., **140**(12), p. 121012.